Supporting Information

Two-Sided Asymmetric Nanofluidic Membrane for Enhanced Ion Transport and Osmotic Energy Harvesting

Qijun Zheng,[a] Yue Shen,[a] Junjian Lu,[a] Yan Xu,[b] Xing-Hua Xia,[c] Chen Wang[a]*

[a]Jiangsu Collaborative Innovation Center of Biomedical Functional Materials, Jiangsu Key Laboratory of New Power Batteries, School of Chemistry and Materials Science, Nanjing Normal University, Nanjing 210023, China

[b]Department of Chemical Engineering, Graduate School of Engineering, Osaka Prefecture University, Sakai, Osaka 599-8570, Japan

[c]State Key Laboratory of Analytical Chemistry for Life Science, School of Chemistry and Chemical Engineering, Nanjing University, Nanjing 210023, China

*To whom correspondence should be addressed: wangchen@njnu.edu.cn (C. Wang)

Table of Contents:

Figure S30. Infrared camera photos and the corresponding temperature change of the Nafion/AAO membrane irradiated with light on and off at different times (light intensity: 200 mW cm^{-2}).
Figure S31. (A) UV-vis spectra of the $Ti_3C_2T_x$ MXene dispersions. (B) UV-vis diffuse reflection spectra of the $Ti_3C_2T_x$ MXene dispersions.
Figure S32. Infrared camera images showing temperature variations of the MXene/AAO/Nafion membrane in aqueous solution.
Figure S33. The I-T curve of (A) AAO, (B) Nafion/AAO, (C) MXene/AAO,(D) MXene/AAO/Nafion in the irradiation "On-Off" experiment (0.01 M KCl, 0.1V).
Figure S34. The I-T curve of the MXene/AAO/Nafion under different light intensity. (A) 50 mW cm^{-2}; (B) 100 mW cm^{-2}; (C) 150 mW cm^{-2}; (D) 200 mW cm^{-2}. (0.01 M KCl 0.1V)
Figure S35. Illustration of ion concentration polarization phenomenonat the surface of a permselective membrane and the proposed strategy for alleviating membrane concentration polarization by a temperature gradient to enhance the thermophoretic mobility of ions.
Figure S36. (A) The low-concentration side was illuminated. (B) Corresponding light-controlled osmotic current. (C) Corresponding current density and power density with and without light irradiation at 0.01/0.5 M NaCl concentration gradient.
Figure S37. (A) The high-concentration side was illuminated. (B) Corresponding light-controlled osmotic current. (C) Corresponding current density and power density with and without light irradiation at 0.01/0.5 M NaCl concentration gradient.
Figure S38. Current density and power density from equilibrium electrolyte solutions system (0.01 M KCl).
Figure S39. Current density under a series of NaCl salinity gradient.
Figure S40. Evaluation of osmotic energy capture performance of pure AAO membrane at 0.01/0.5 M NaCl concentration gradient.
Figure S41. Evaluation of osmotic energy capture performance of the Nafion/AAO membrane at 0.01/0.5 M NaCl concentration gradient.
Figure S42. Evaluation of osmotic energy capture performance of the Nafion/AAO membrane at 0.01/0.5 M NaCl concentration gradient.
Figure S43. Power density of three different membranes with and without light irradiation.
Figure S44. (A) Current density and (B) power density of the MXene/AAO/Nafion membrane under a series of KCl concentration gradient. (C) Current density and (D) power density of the MXene/AAO/Nafion membrane with light irradiation under a series of KCl concentration gradient.
Figure S45. (A) Current density and (B) power density of the MXene/AAO/Nafion membrane under different light irradiation. Concentration gradient is 0.01/0.5 M NaCl.
Figure S46. (A) Current density and (B) power density of the MXene/AAO/Nafion membrane under different working area at 50-fold salinity gradient. (C) Current density and (D) power density of the MXene/AAO/Nafion membrane under different working area with light irradiation at 50-fold salinity gradient.
Figure S47. (A)Current density and (B)power density of the Nafion/AAO membrane under different working area at 50-fold NaCl salinity gradient.
Figure 48. (A) Current density and (B) power density of the Nafion/AAO/Nafion membrane under different working area at 50-fold NaCl salinity gradient.
Figure S49. The output power of different membranes under different working area at 50-fold NaCl salinity gradient.
Figure S50. The output power of (A) Nafion/AAO/Nafion, (B) MXene/AAO/Nafion under irradiation and (C) Nafion/AAO under different working area (Percentage decrease in power output with increasing test area).

Figure S51. (A) Current density and (B) power density of the MXene/AAO/Nafion membrane in different pH values. (C) Current density and (D) power density of the MXene/AAO/Nafion membrane in different pH values with light irradiation. Concentration gradient is 50-fold NaCl.
Figure S52. (A) Current density and (B) power density of the MXene/AAO/Nafion membrane under different electrolyte at 50-fold salinity gradient. (C) Current density and (D) power density of the MXene/AAO/Nafion membrane with light irradiation under different electrolyte at 50-fold salinity gradient.
Figure S53. Short-circuit current of the MXene/AAO/Nafion membrane continuously measured for 3600 s. Concentration gradient is 50-fold NaCl.
Figure S54. Stability of the MXene/AAO/Nafion membrane under 50-fold NaCl concentration gradient.
Figure S55. MXene/AAO/Nafion membrane maintain complete structure after immersing in river water for at least 14 days.
Figure S56. The testing stability of the MXene/AAO/Nafion membrane under real river water/seawater condition.
Figure S57. Stability of the MXene/AAO/Nafion membrane. (A-H) Osmotic energy harvesting performance at 1; 3; 5; 7; 9; 11; 13; 14 days under real river water/seawater condition.
Figure S58. SEM characterization of the MXene/AAO/Nafion membrane after 14-day real river water/seawater testing and water cleaning.
Figure S59. Schematic illustration of tandem cell stacks for voltage amplification.
Figure S60. 10 units of the MXene/AAO/Nafion membrane-based power generators can power a timepiece.
Table S1. Corresponding V_{oc}, E_{redox}, and E_{diff} of the MXene/AAO/Nafion membrane under different KCl concentration gradients.
Table S2. The dependence of Debye screening length on the concentrations of KCl solution.
Table S3. The corresponding values of V_{oc}, E_{redox}, and E_{diff} under 50-fold NaCl concentration gradient.
Table S4. Comparison of the value of t_+ under 50-fold NaCl concentration gradient.
Table S5. Comparison of the various nanofluidic devices performance for the salinity gradient energy conversion.
Table S6. Comparison of the voltage of 10-units with previously reported devices at a salinity gradient of 50-fold NaCl.

Supporting Figures and Tables:

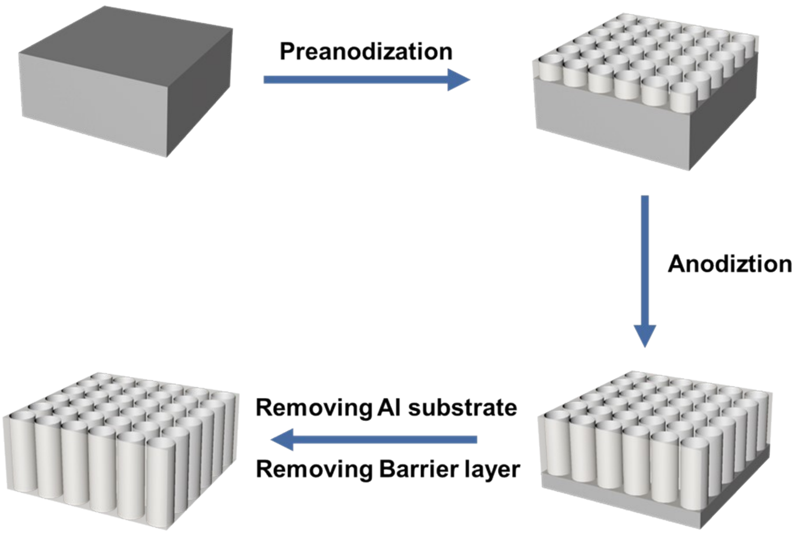

Figure S1. Schematic illustration of the two-step anodization procedure we employed for the fabrication of alumina nanochannel membrane (AAO) with highly ordered straight channels.

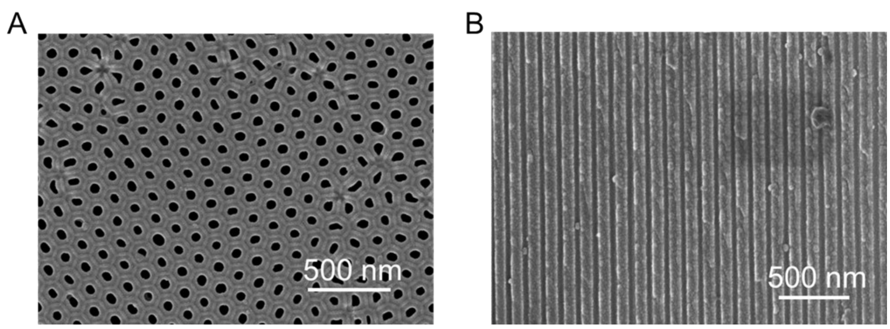

Figure S2. SEM images of the top and cross-section of pure AAO membrane.

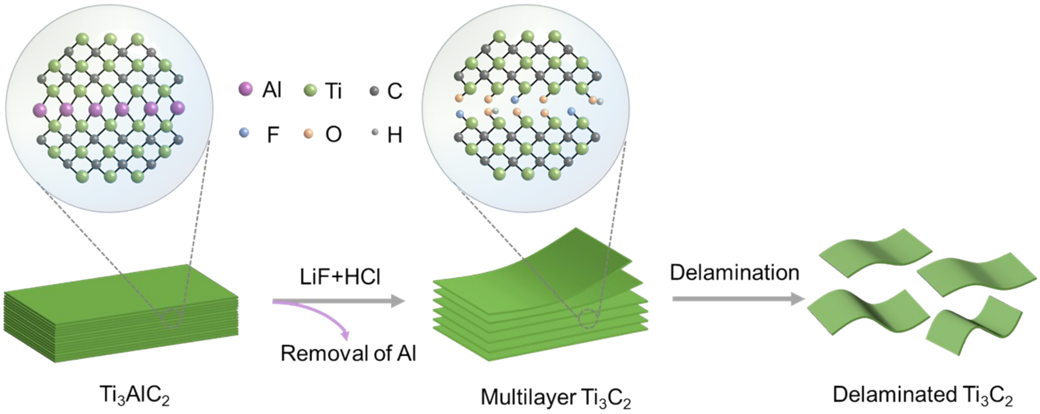

Figure S3. Principle of $Ti_3C_2T_x$ nanosheet preparation.

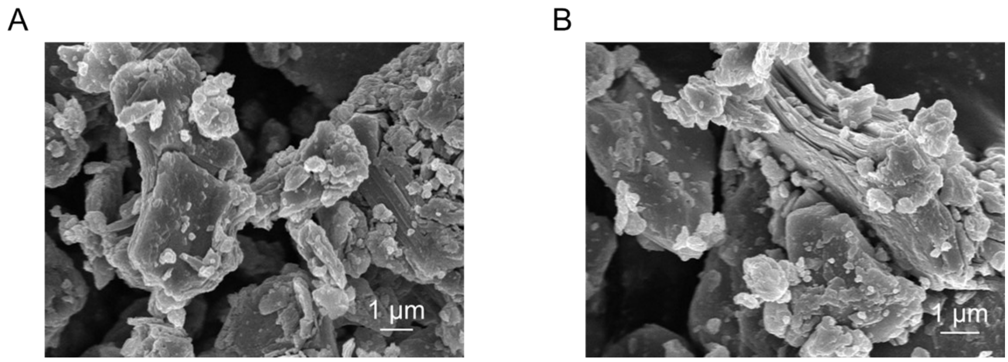

Figure S4. SEM image of Ti_3AlC_2.

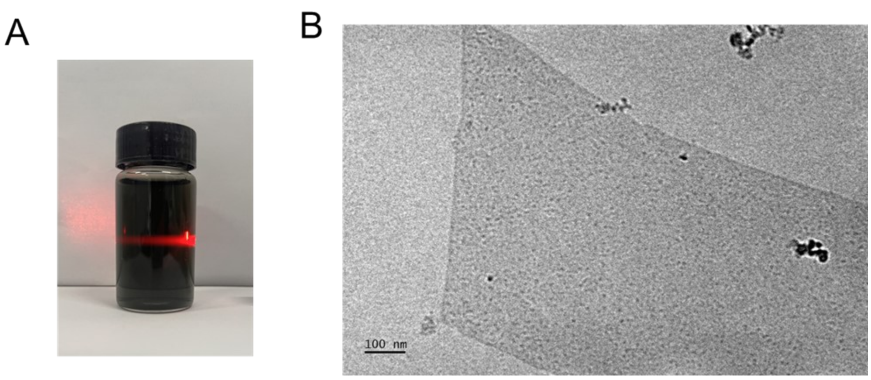

Figure S5. (A) Photograph of $Ti_3C_2T_x$ dispersion. (B) TEM image of $Ti_3C_2T_x$

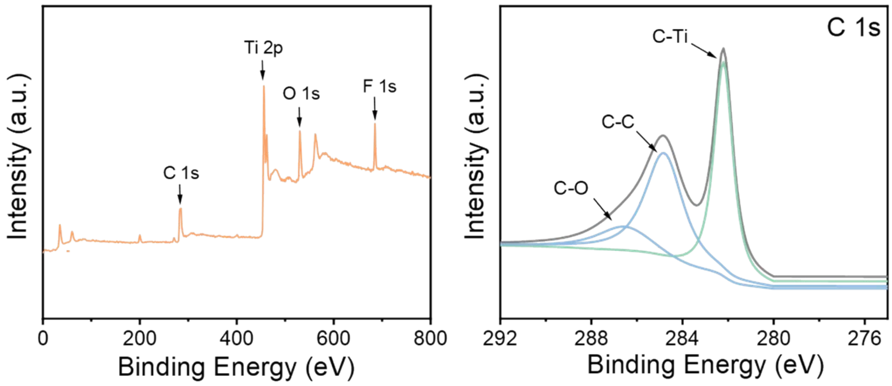

Figure S6. The XPS spectra of $Ti_3C_2T_x$.

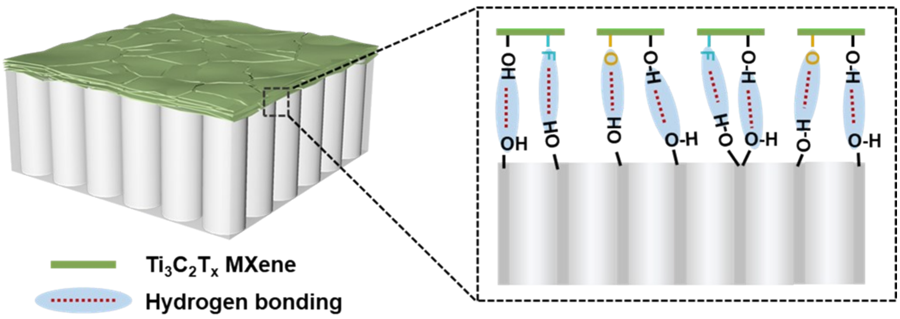

Figure S7. Schematic illustration for the interaction of interface between MXene and AAO.

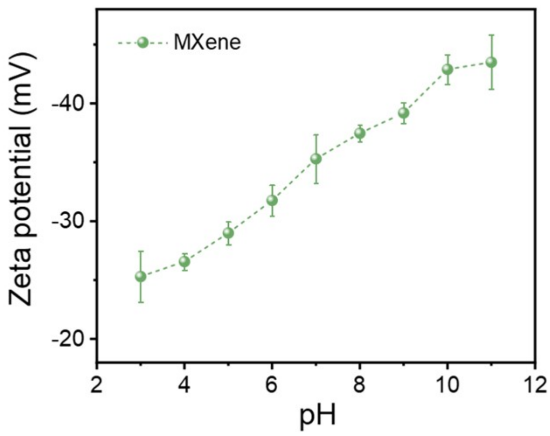

Figure S8. Zeta potential of the MXene under different pH values.

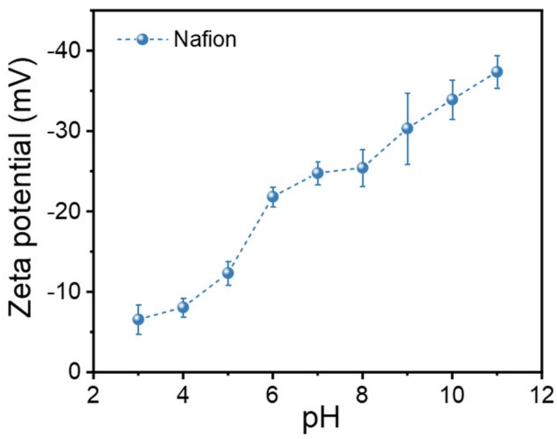

Figure S9. Zeta potential of the Nafion under different pH values.

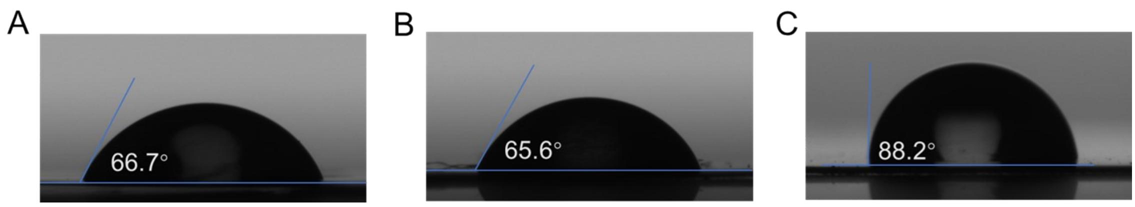

Figure S10. Contact angle of (A) AAO; (B) MXene side; (C) Nafion side.

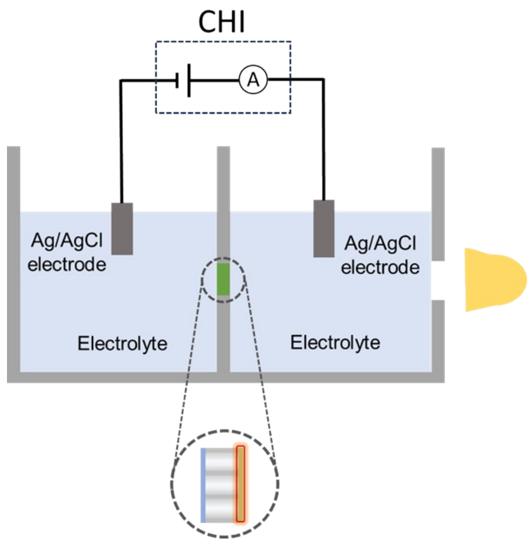

Figure S11. Schematic illustration of the experimental setup for electrochemical measurements.

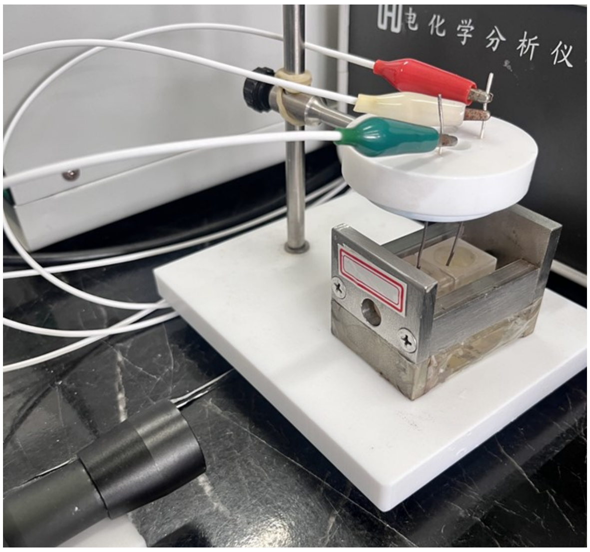

Figure S12. The camera photo of the practical testing device.

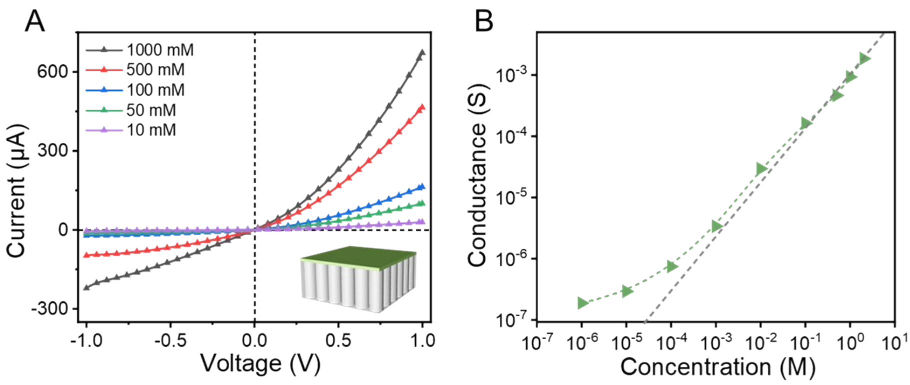

Figure S13. (A) I-V curves of the MXene/AAO membrane in various concentrations of KCl solutions. (B) The conductance in various concentration of KCl solutions (ranging from 1×10^{-6} to 2 M).

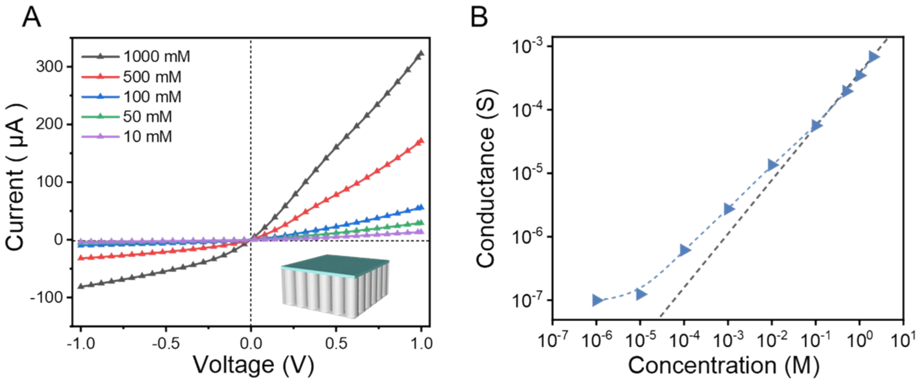

Figure S14. (A) I-V curves of the Nafion/AAO membrane in various concentrations of KCl solutions. (B) The conductance in various concentration of KCl solutions (ranging from 1×10^{-6} to 2 M).

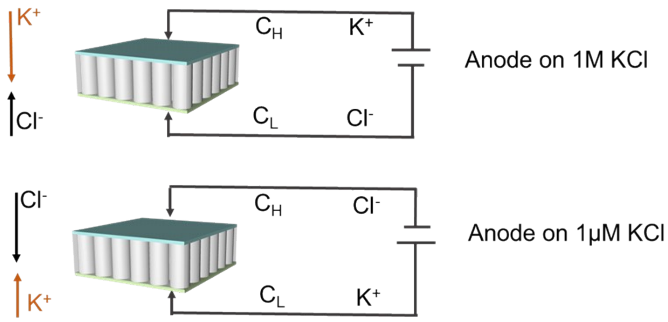

Figure S15. Schematic diagram illustrating the ion selectivity of nanofluidic membrane investigated through electrochemical technique.

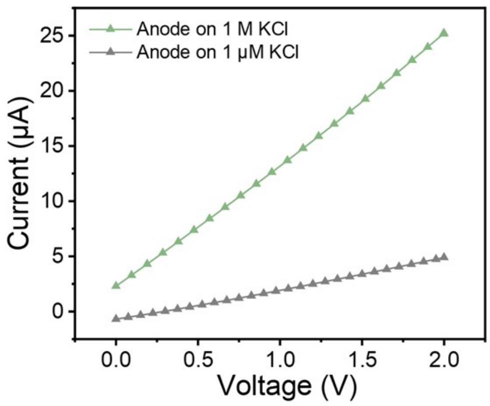

Figure S16. I-V curves of the MXene/AAO membrane in two different salt concentrations. The green curve represents the current contributed by K^+ and the gray curve represents the current contributed by Cl^-

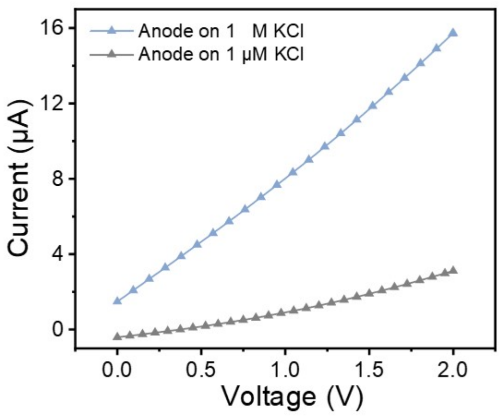

Figure S17. I-V curves of the Nafion/AAO membrane in two different salt concentrations. The blue curve represents the current contributed by K^+ and the orange curve represents the current contributed by Cl^-.

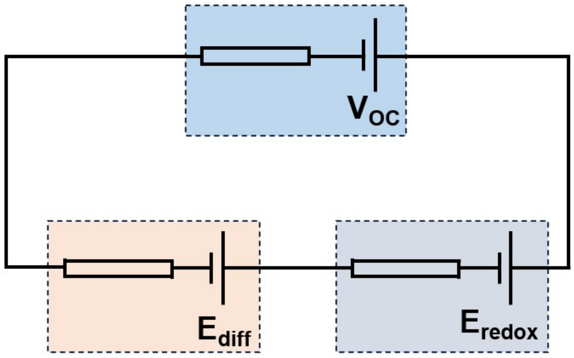

Figure S18. Equivalent circuit diagram demonstrated of the osmotic energy output system.

The energy conversion property of the MXene/AAO/Nafion membrane was estimated by collecting I-V curves under different transmembrane concentration gradients. The voltage was scanned from -0.4 V to 0.4 V with a step of 0.04 V/S. The short-circuit current (I_{SC}) and open-circuit potential (V_{OC}) can be directly read from the intercepts of the characteristic I-V curves on the current and voltage axes, respectively. The measured V_{OC} includes two parts: the Redox potential (E_{redox}) and the diffusion potential (E_{diff}). E_{redox} is generated by unequal potential drop at the electrode-electrolyte interface, and E_{diff} is contributed by the concentration gradient induced charge separation across the membrane.

E_{diff} can be calculated from Equation S1

$$E_{diff} = V_{oc} - E_{redox} \qquad \text{Equation S1}$$

The calibration of E_{redox} was performed using the same electrochemical half-cell as those in the energy conversion experiment, but a non-selective AAO membrane was used.

The transference number t_+ is calculated from Equation S2:

$$t_+ = \frac{1}{2}\left(\frac{E_{diff}}{\frac{RT}{zF}ln\frac{\gamma_{C_H}C_H}{\gamma_{C_L}C_L}} + 1\right) \qquad \text{Equation S2}$$

R, T, z, F, and c represent separately the gas constant, temperature, charge number, Faraday constant, and mean activity coefficient, respectively.[1]

The energy conversion efficiency (η) can be calculated from Equation S3:[2]

$$\eta_{max} = \frac{(2t_+ - 1)^2}{2} \qquad \text{Equation S3}$$

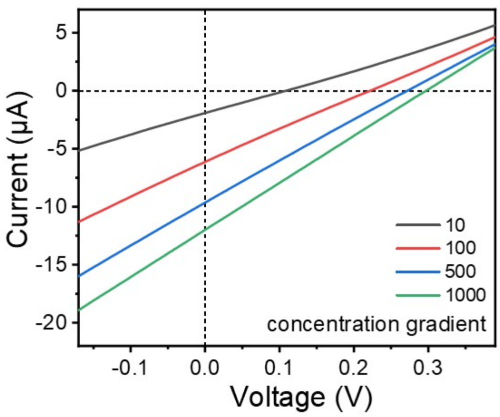

Figure S19. I-V curves of the MXene/AAO/Nafion membrane under a series of KCl concentration gradients.

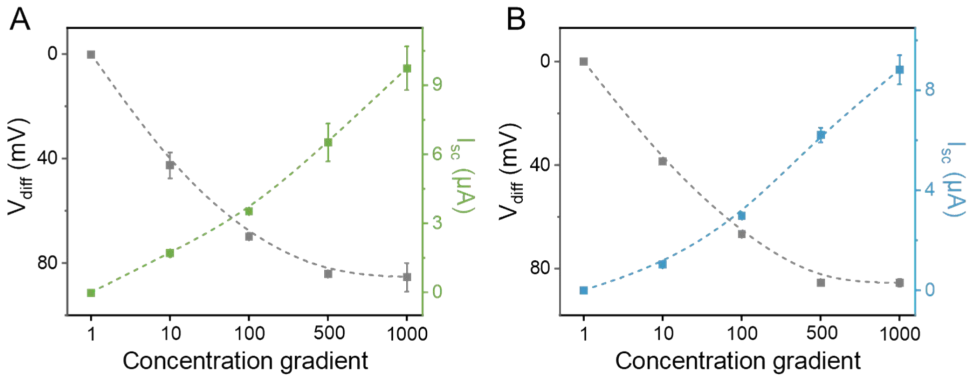

Figure S20. (A) I_{SC} and E_{diff} of the MXene/AAO membrane at a range of KCl salinity gradients. MXene side contacts with 1 mM KCl and AAO side of the KCl concentration was gradually increased from 1 mM to 1 M. (B) I_{SC} and E_{diff} of the Nafion/AAO membrane at a range of KCl salinity gradients. Nafion side contacts with 1 mM KCl and AAO side of the KCl concentration was gradually increased from 1 mM to 1 M.

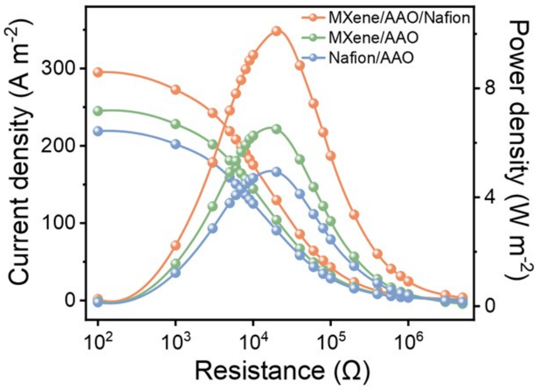

Figure S21. Current density and power density of different membranes at 0.01/0.5 M NaCl concentration gradient.

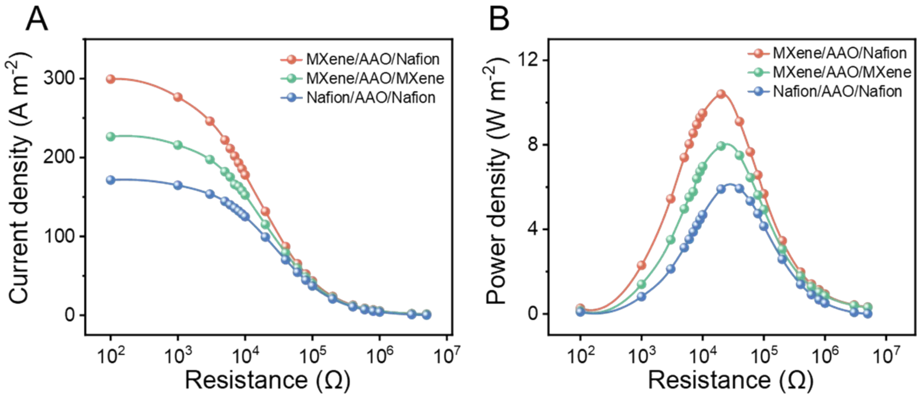

Figure S22. (A) Current density and (B) Power density of MXene/AAO/Nafion, MXene/AAO/MXene and Nafion/AAO/Nafion membranes.

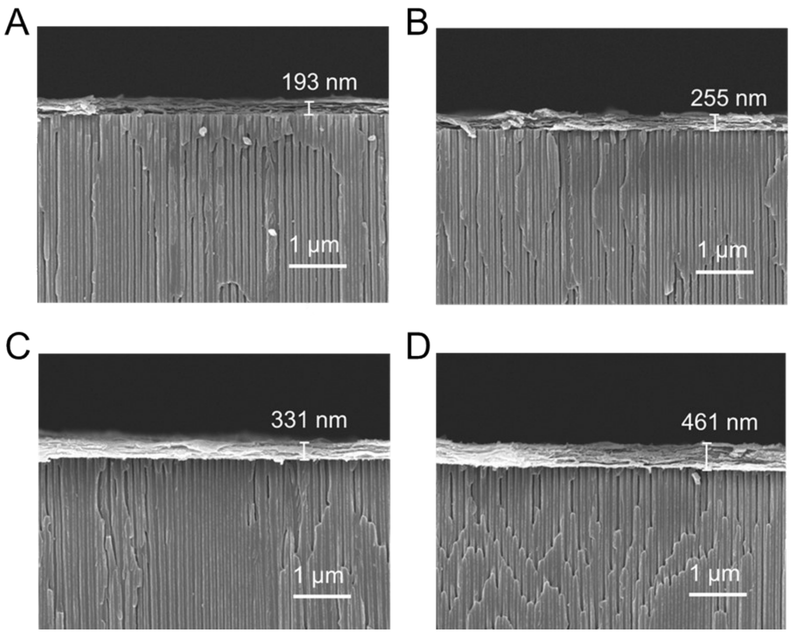

Figure S23. SEM images of the cross-section (A-D) of MXene/AAO with different thickness. In figure A-D, 4ml,6ml,8ml,10ml MXene dispersions were used, respectively.

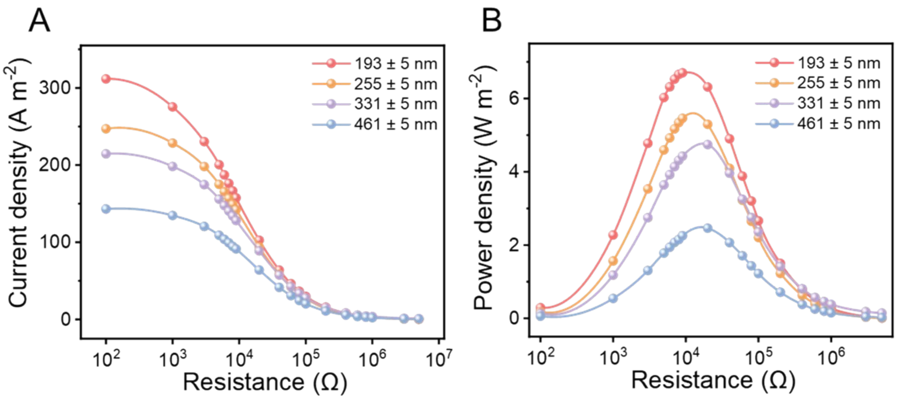

Figure S24. (A) Current density and (B) Power density of the MXene/AAO with different thickness under a 50-fold NaCl gradient.

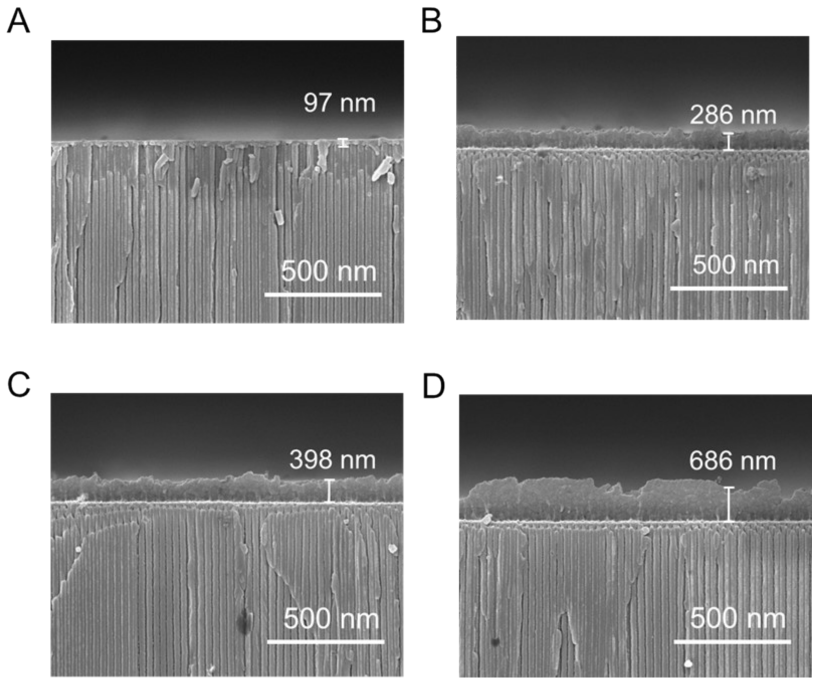

Figure S25. SEM images of the cross-section (A-D) of Nafion/AAO with different thickness. In figure A-D, spin coating 1, 2, 3, and 4 times, respectively.

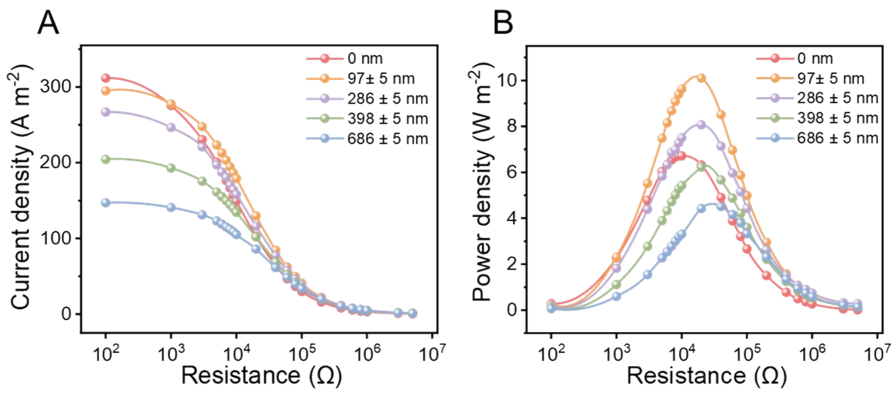

Figure S26. (A) Current density and (B) Power density of the MXene/AAO/Nafion different thickness of Nafion layer under a 50-fold NaCl gradient.

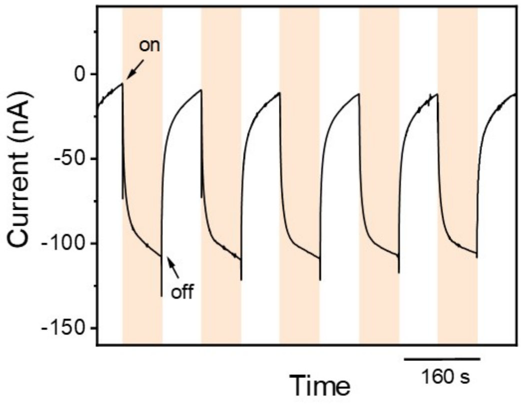

Figure S27. Photocurrent through the MXene/AAO membrane under light irradiation (0.01 M KCl).

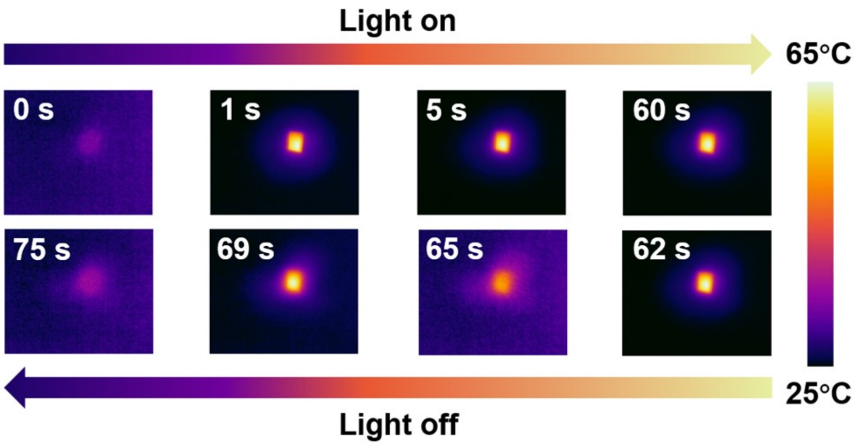

Figure S28. Infrared camera photos and the corresponding temperature change of the MXene/AAO/Nafion membrane irradiated with light on and off at different times (light intensity: 200 mW cm^{-2}).

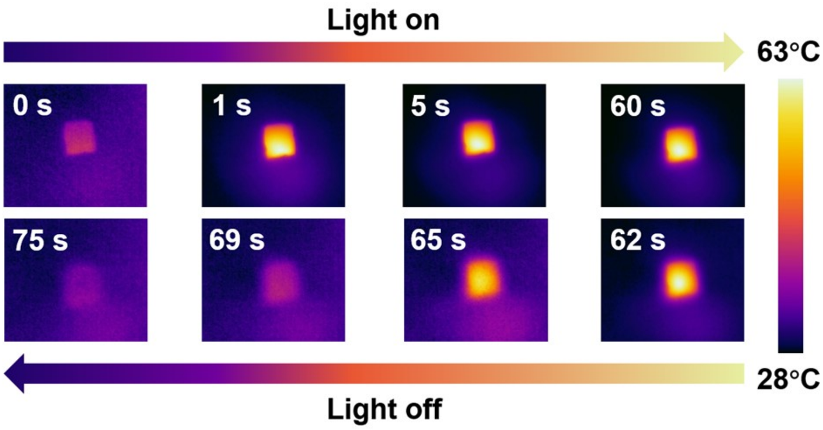

Figure S29. Infrared camera photos and the corresponding temperature change of the MXene/AAO membrane irradiated with light on and off at different times (light intensity: 200 mW cm^{-2}).

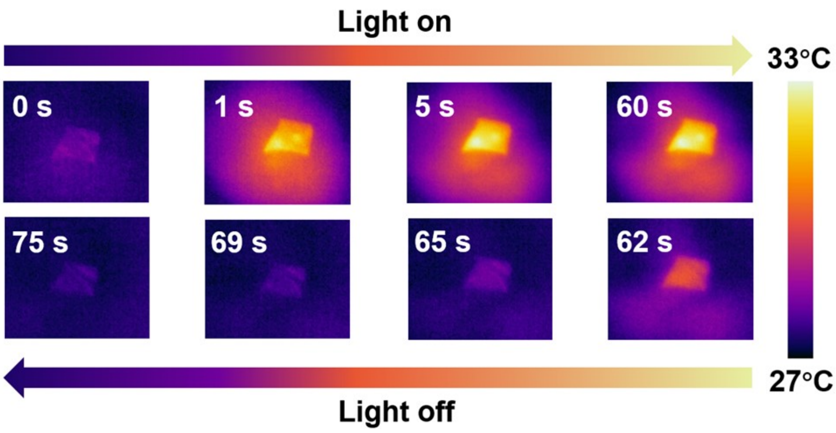

Figure S30. Infrared camera photos and the corresponding temperature change of the Nafion/AAO membrane irradiated with light on and off at different times (light intensity: 200 mW cm^{-2}).

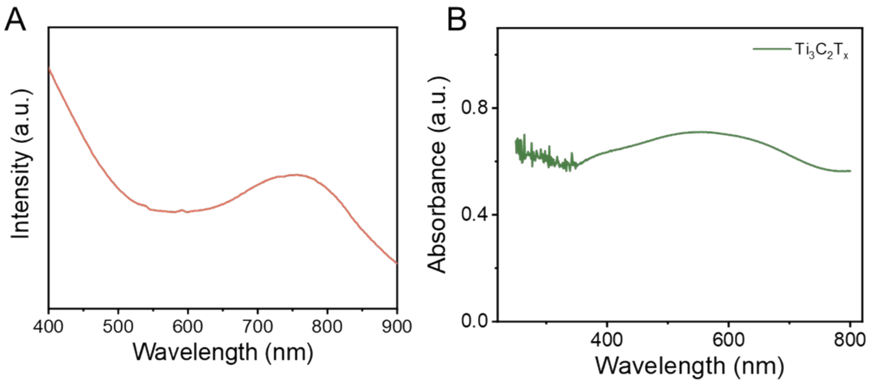

Figure S31. (A) UV-vis spectra of the $Ti_3C_2T_x$ MXene dispersions. (B) UV-vis diffuse reflection spectra of the $Ti_3C_2T_x$ MXene dispersions.

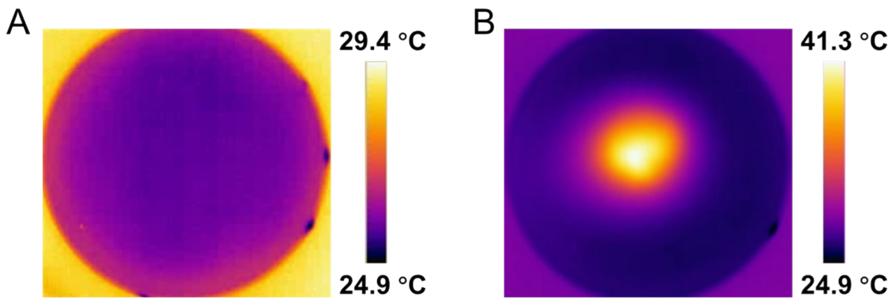

Figure S32. Infrared camera images showing temperature variations of the MXene/AAO/Nafion membrane in aqueous solution. (A) Without light irradiation, (B) After 5 minutes of light irradiation.

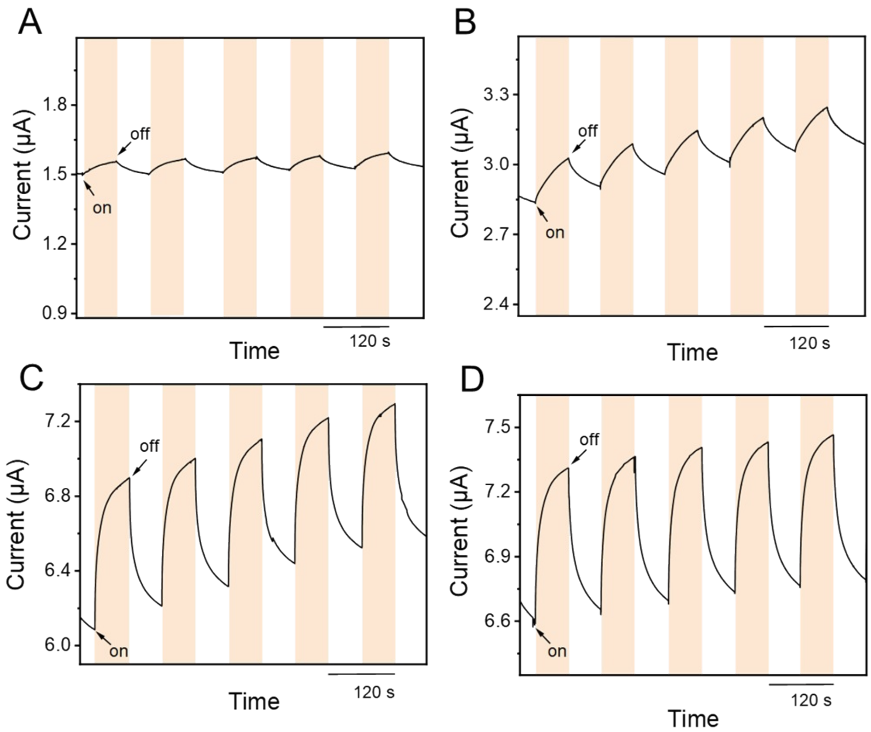

Figure S33. The I-T curve of (A) AAO, (B) Nafion/AAO, (C) MXene/AAO,(D) MXene/AAO/Nafion in the irradiation "On-Off" experiment (0.01 M KCl, 0.1V).

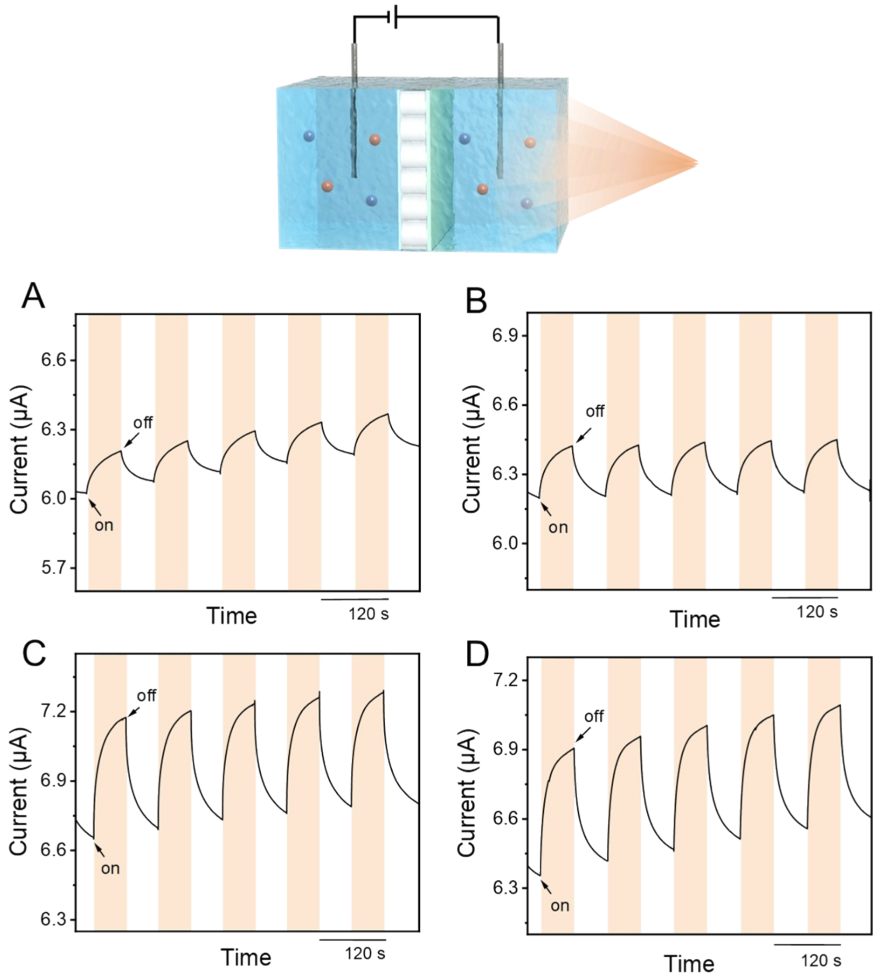

Figure S34. The I-T curve of the MXene/AAO/Nafion under different light intensity. (A) 50 mW cm^{-2}; (B) 100 mW cm^{-2}; (C) 150 mW cm^{-2}; (D) 200 mW cm^{-2}. (0.01 M KCl 0.1V)

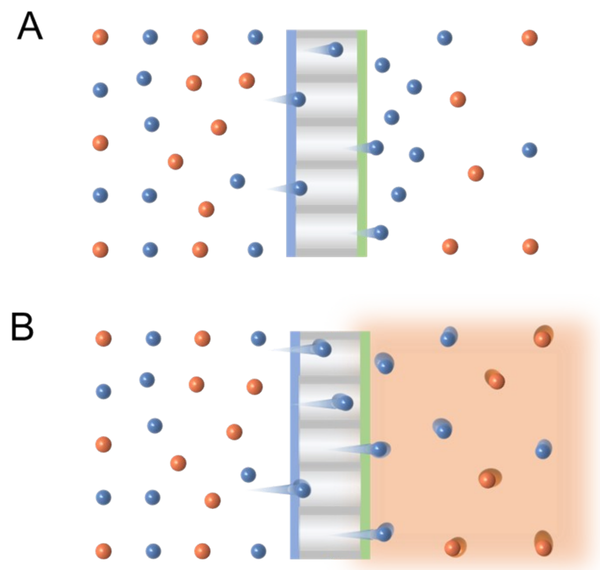

Figure S35. Illustration of ion concentration polarization phenomenon (ICP) at the surface of a permselective membrane and the proposed strategy for alleviating ICP by a temperature gradient to enhance the thermophoretic mobility of ions. (A) Ion transport through a permselective membrane, which is accompanied by the occurrence of ICP. (B) Ion transport through a permselective membrane with alleviated ICP by increasing the hydrodynamic convection effects.

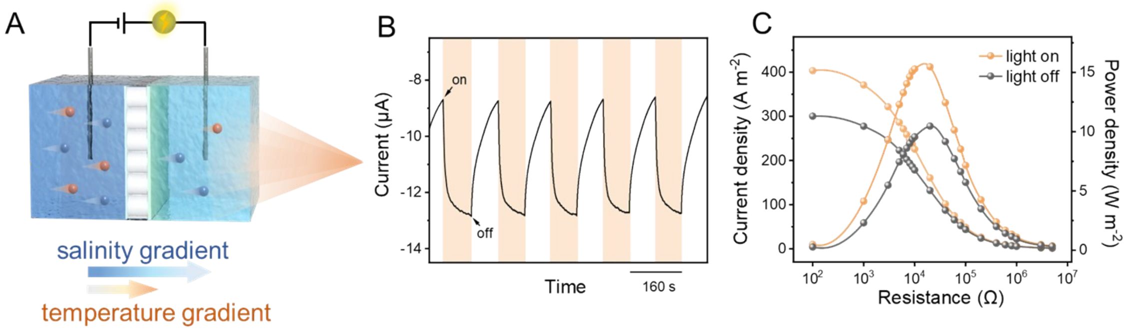

Figure S36. (A) The low-concentration side was illuminated. (B) Corresponding light-controlled osmotic current. (C) Corresponding current density and power density with and without light irradiation at 0.01/0.5 M NaCl concentration gradient.

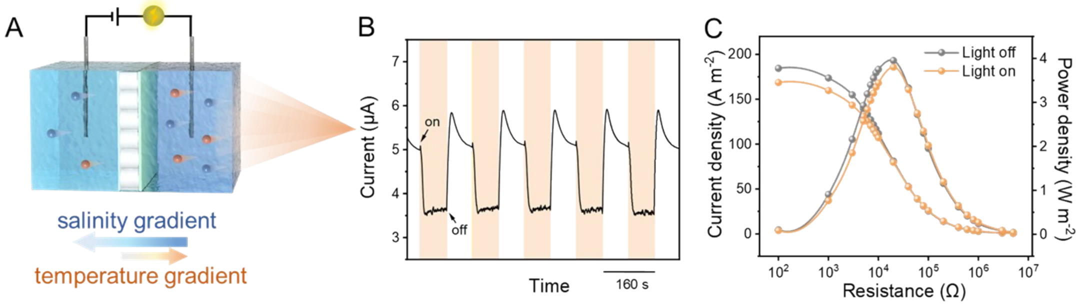

Figure S37. (A) The high-concentration side was illuminated. (B) Corresponding light-controlled osmotic current. (C) Corresponding current density and power density with and without light irradiation at 0.01/0.5 M NaCl concentration gradient.

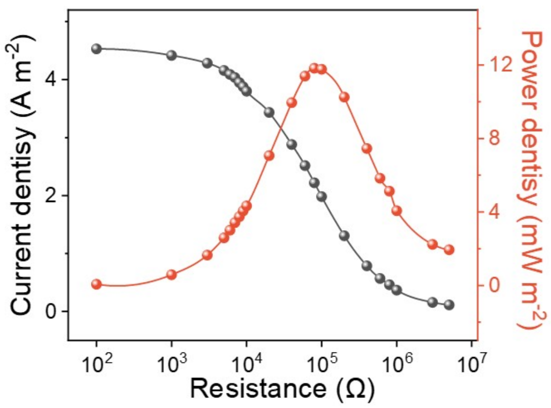

Figure S38. Current density and power density from equilibrium electrolyte solutions system (0.01 M KCl).

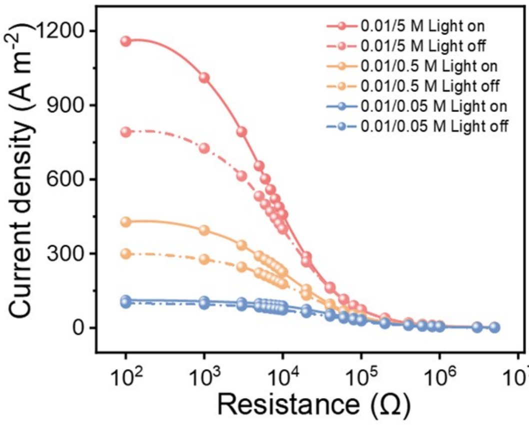

Figure S39. Current density under a series of NaCl salinity gradient.

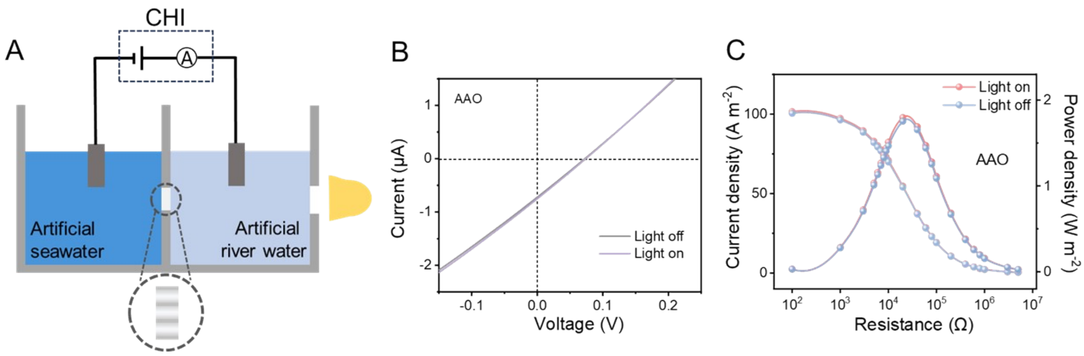

Figure S40. Evaluation of osmotic energy capture performance of pure AAO membrane at 0.01/0.5 M NaCl concentration gradient. (A) Schematic diagram of osmotic energy harvesting of pure AAO membrane. (B) I-V curves of the pure AAO membrane with and without light irradiation. (C) Current density and power density of the pure AAO membrane with and without light irradiation.

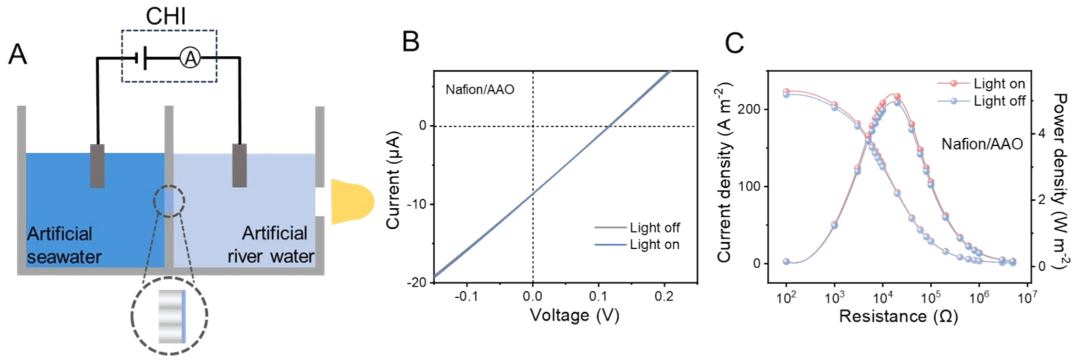

Figure S41. Evaluation of osmotic energy capture performance of the Nafion/AAO membrane at 0.01/0.5 M NaCl concentration gradient. (A) Schematic diagram of osmotic energy harvesting of Nafion/AAO membrane. (B) I-V curves of the Nafion/AAO membrane with and without light irradiation. (C) Current density and power density of the Nafion/AAO membrane with and without light irradiation.

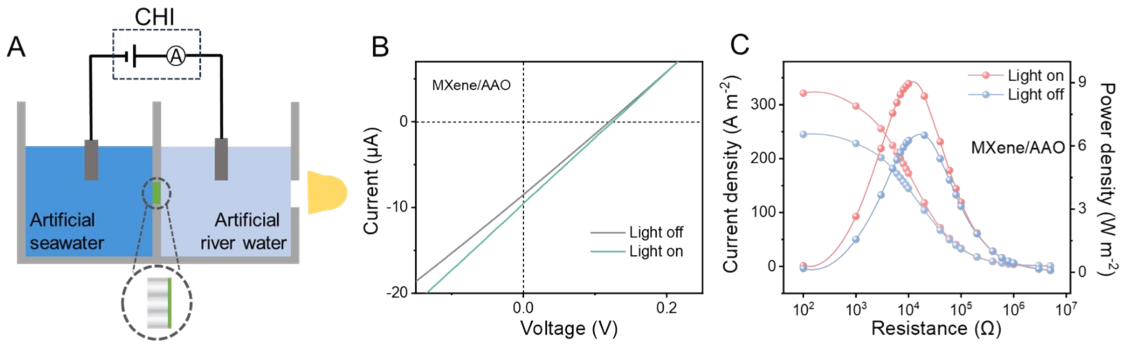

Figure S42. Evaluation of osmotic energy capture performance of the MXene/AAO membrane at 0.01/0.5 M NaCl concentration gradient. (A) Schematic diagram of osmotic energy harvesting of MXene/AAO membrane. (B) I-V curves of the MXene/AAO membrane with and without light irradiation. (C) Current density and power density of the Nafion/AAO membrane with and without light irradiation.

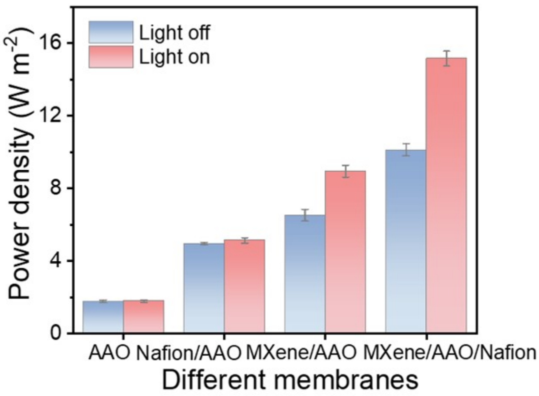

Figure S43. Power density of three different membranes with and without light irradiation.

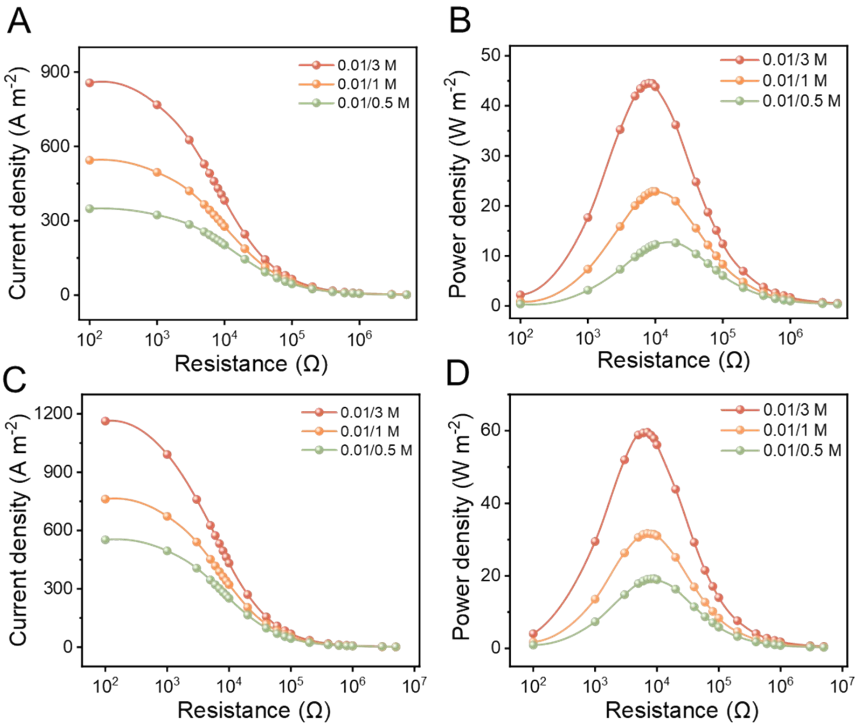

Figure S44. (A) Current density and (B) power density of the MXene/AAO/Nafion membrane under a series of KCl concentration gradients. (C) Current density and (D) power density of the MXene/AAO/Nafion membrane with light irradiation under a series of KCl concentration gradients.

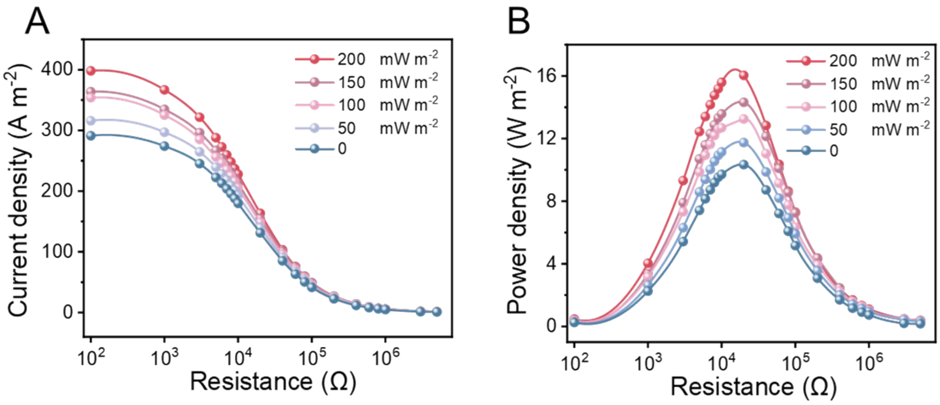

Figure S45. (A) Current density and (B) power density of the MXene/AAO/Nafion membrane under different light irradiation. Concentration gradient is 0.01/0.5 M NaCl.

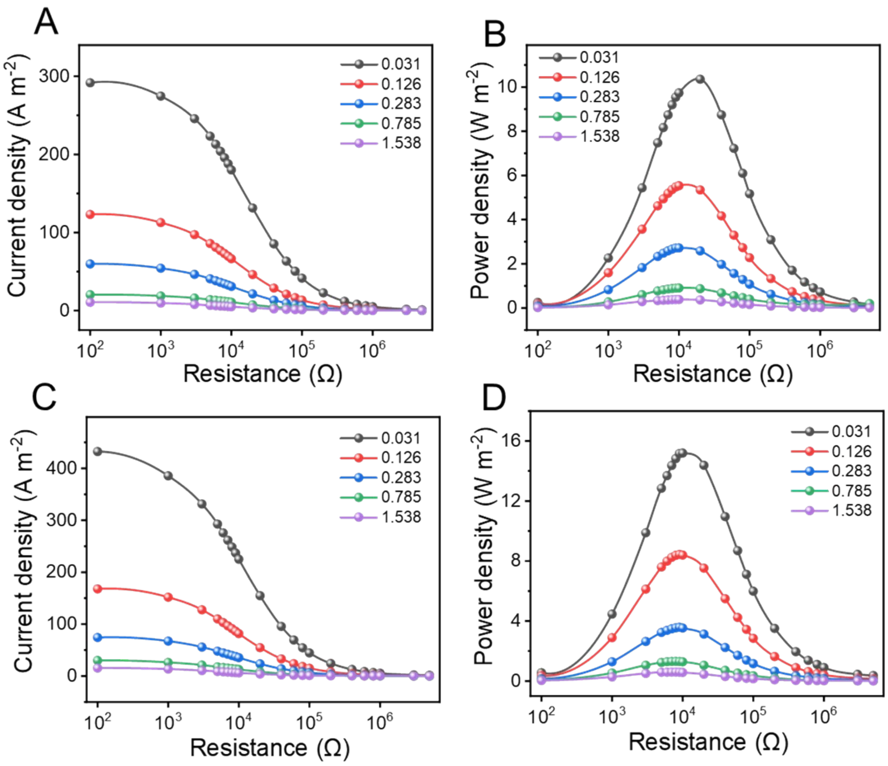

Figure S46. (A) Current density and (B) power density of the MXene/AAO/Nafion membrane under different working area at 50-fold NaCl salinity gradient. (C) Current density and (D) power density of the MXene/AAO/Nafion membrane under different working area with light irradiation at 50-fold NaCl salinity gradient.

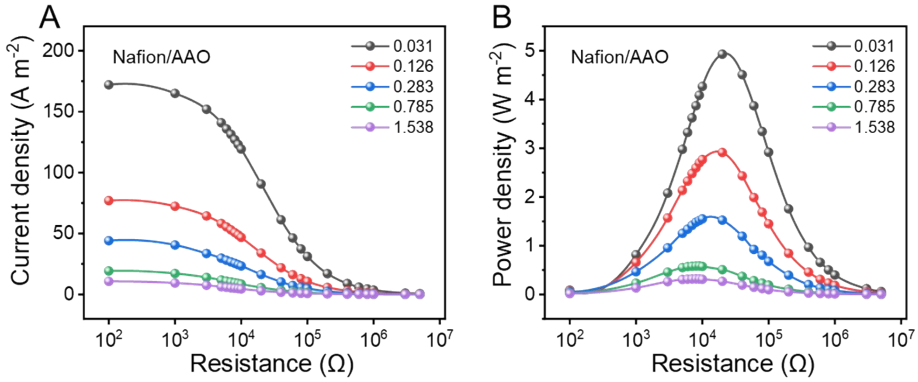

Figure S47. (A)Current density and (B)power density of the Nafion/AAO membrane under different working area at 50-fold NaCl salinity gradient.

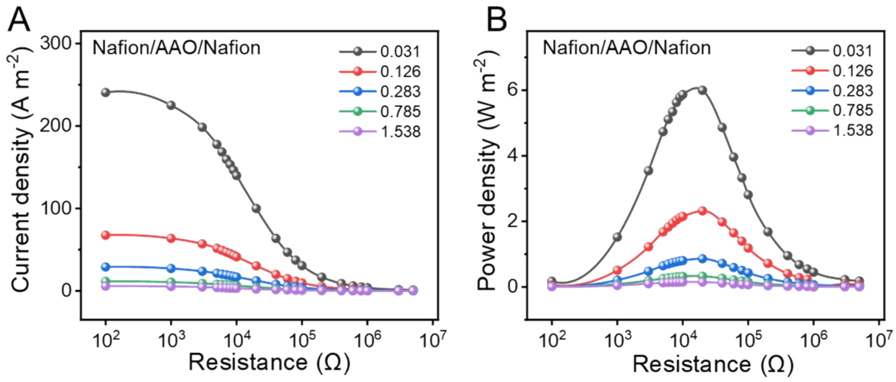

Figure S48. (A) Current density and (B)power density of the Nafion/AAO/Nafion membrane under different working area at 50-fold NaCl salinity gradient.

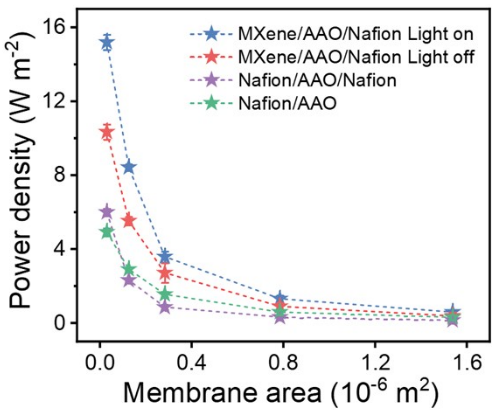

Figure S49. The output power of different membranes under different working area at 50-fold NaCl salinity gradient.

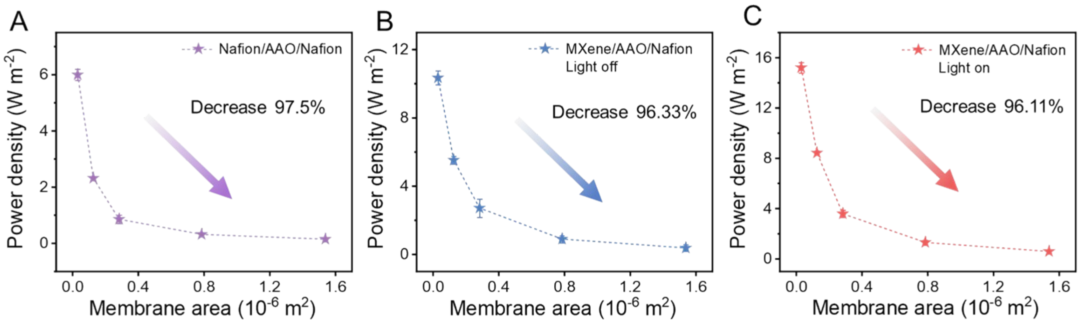

Figure S50. The output power of (A) Nafion/AAO/Nafion, (B) MXene/AAO/Nafion under irradiation and (C) Nafion/AAO under different working area. (Percentage decrease in power output with increasing test area)

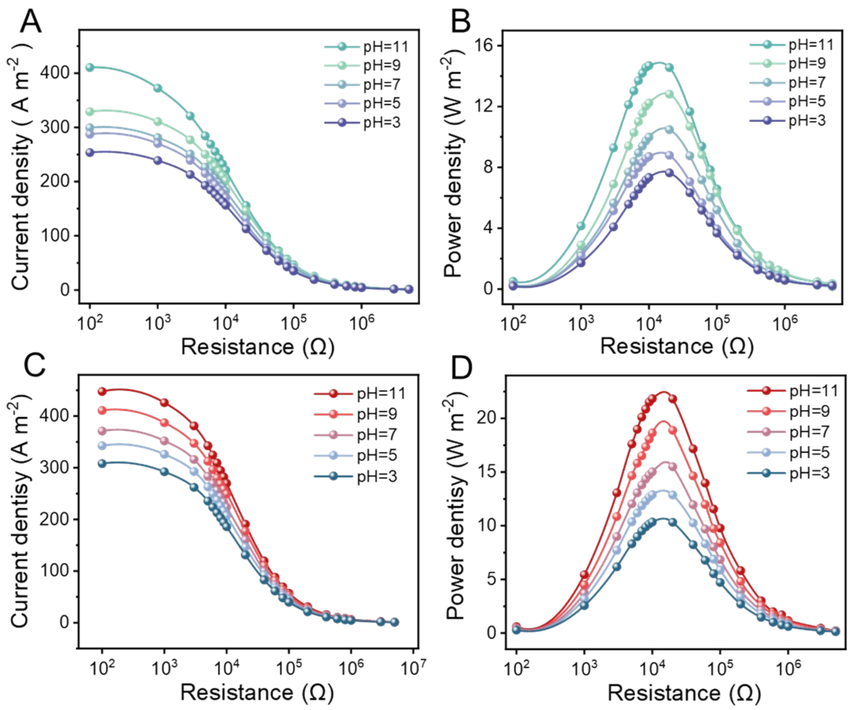

Figure S51. (A) Current density and (B) power density of the MXene/AAO/Nafion membrane in different pH values. (C) Current density and (D) power density of the MXene/AAO/Nafion membrane in different pH values with light irradiation. Concentration gradient is 50-fold NaCl.

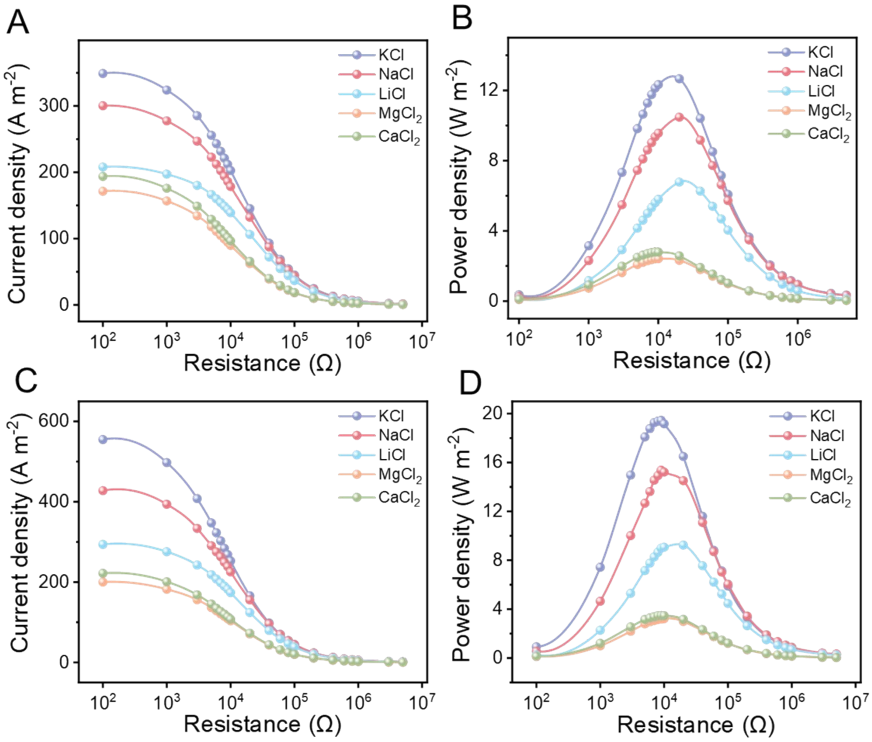

Figure S52. (A) Current density and (B) power density of the MXene/AAO/Nafion membrane under different electrolyte at 50-fold salinity gradient. (C) Current density and (D) power density of the MXene/AAO/Nafion membrane with light irradiation under different electrolyte at 50-fold salinity gradient.

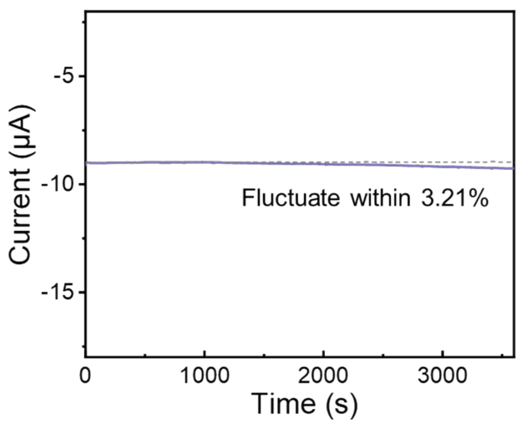

Figure S53. Short-circuit current of the MXene/AAO/Nafion membrane continuously measured for 3600 s. Concentration gradient is 50-fold NaCl.

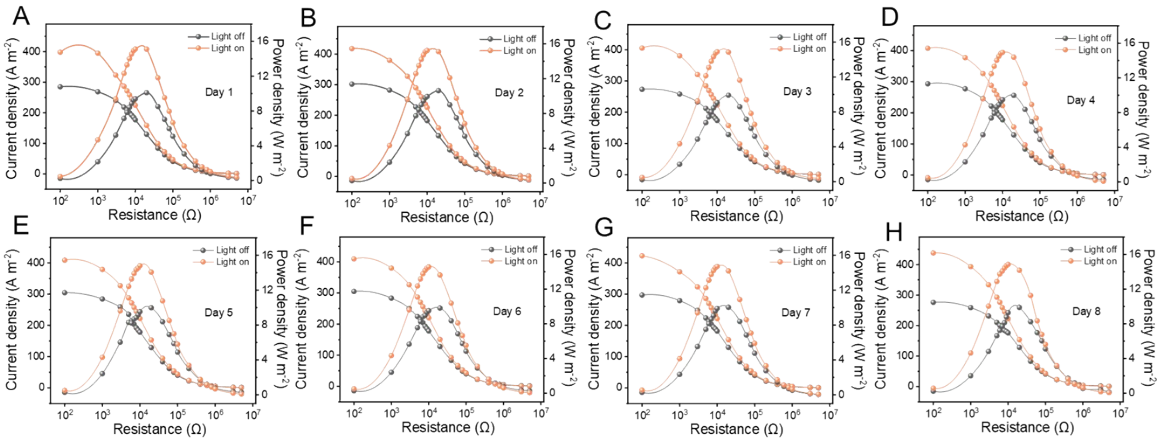

Figure S54. Stability of the MXene/AAO/Nafion membrane under 50-fold NaCl concentration gradient.

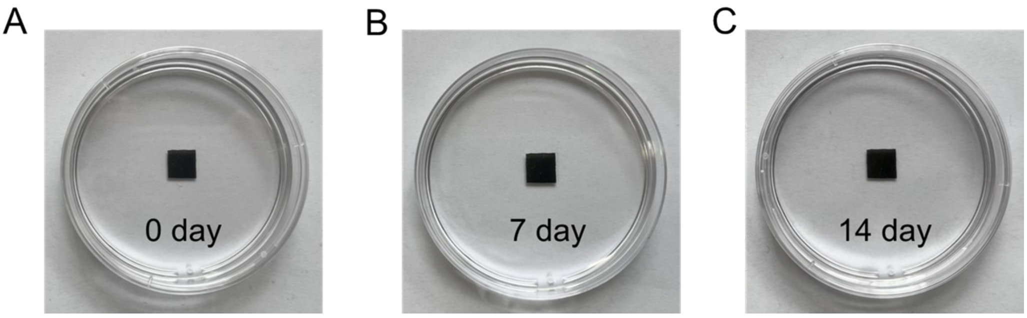

Figure S55. MXene/AAO/Nafion membrane maintain complete structure after immersing in river water for at least 14 days.

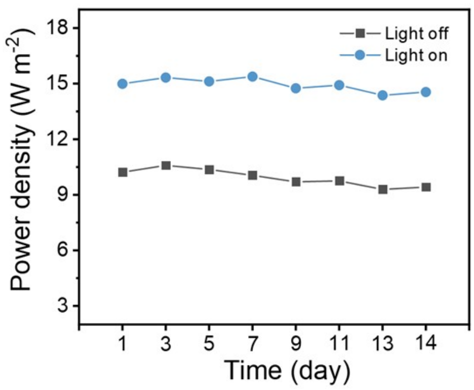

Figure S56. The testing stability of the MXene/AAO/Nafion membrane under real river water/seawater condition.

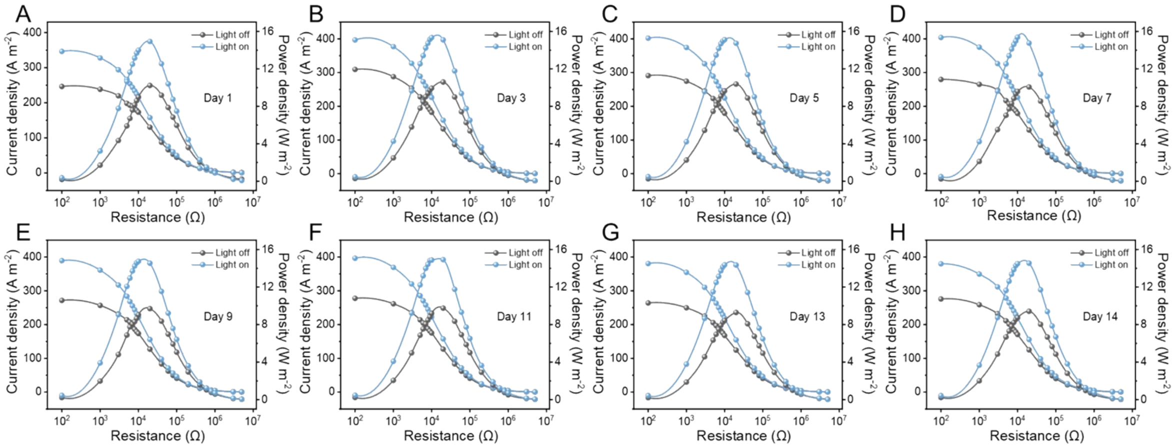

Figure S57. Stability of the MXene/AAO/Nafion membrane. (A-H) Osmotic energy harvesting performance at 1; 3; 5; 7; 9; 11; 13; 14 days under real river water/seawater condition.

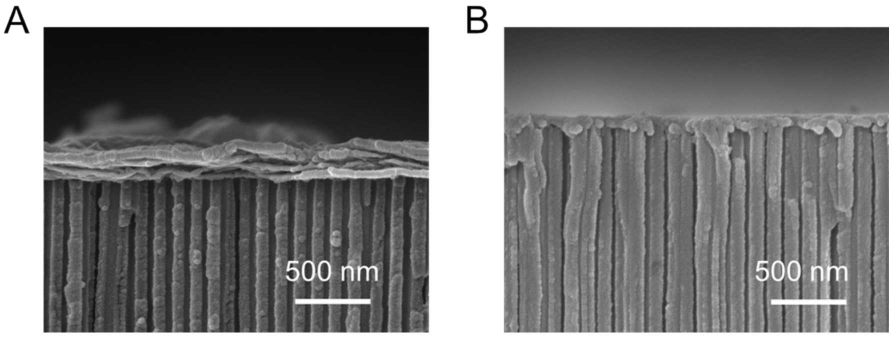

Figure S58. SEM characterization of the MXene/AAO/Nafion membrane after 14-day real river water/seawater testing and water cleaning. (A) Cross-sectional image of MXene layer. (B) Cross-sectional image of Nafion layer.

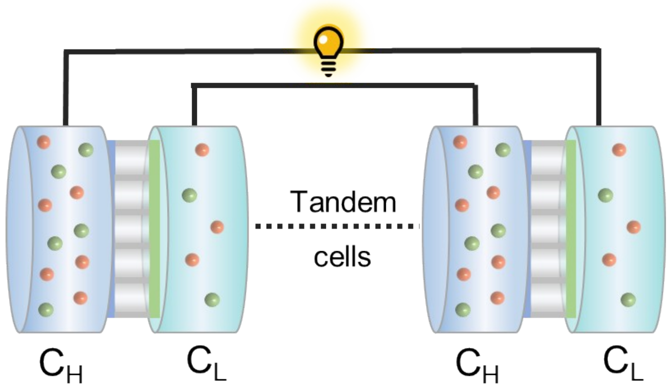

Figure S59. Schematic illustration of tandem cell stacks for voltage amplification.

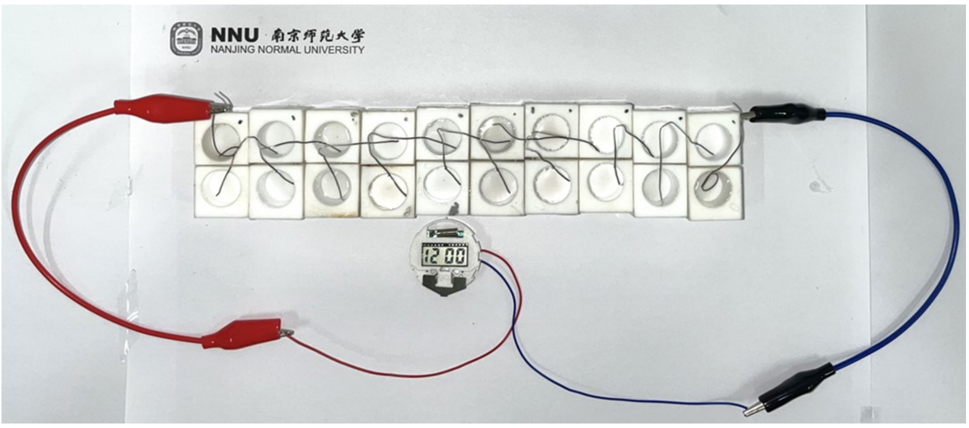

Figure S60. 10 units of the MXene/AAO/Nafion membrane-based power generators can power a timepiece.

Table S1. Corresponding V_{oc}, E_{redox}, and E_{diff} of the MXene/AAO/Nafion membrane under different KCl concentration gradients.

c_{max}/c_{min}	I_{SC}, μA	V_{OC}, mV	E_{redox}, mV	E_{diff}, mV
1 mM/1 mM	Set to 0			
10 mM/1 mM	1.92	111.1	56	55.1
100 mM/1 mM	6.13	217	107.7	109.3
500 mM/1 mM	9.65	276.5	139.3	137.2
1 M/1 mM	11.99	303.7	153.5	150.2

Table S2. The dependence of Debye screening length on the concentrations of KCl solution.

Electrolyte concentration (mM)	1000	500	100	10	1
Debye length (nm)[a]	0.3	0.42	0.96	3.03	9.59

[a]The Debye length is defined as

$$\lambda_D = \sqrt{\frac{\varepsilon_r \varepsilon_0 \kappa_B T}{2 N_A I' e^2}}$$

where ε_r and ε_0 are the vacuum and relative permittivity, respectively, k_B is the Boltzmann constant, T is the absolute temperature, e is the elementary charge, N_A is the Avogadro number, and I' is the ionic strength of the solution.

Table S3. The corresponding values of V_{oc}, E_{redox}, and E_{diff} under 50-fold NaCl concentration gradient.

Membranes	V_{OC}, mV	E_{diff}, mV	t_+	η (%)
MXene/AAO	120	48	0.76	13.5
Nafion/AAO	117	45	0.74	11.5
MXene/AAO/Nafion	154	82	0.95	40.5

Table S4. Comparison of the value of t_+ under 50-fold NaCl concentration gradient.

Membrane	**t_+**	**Test Condition**	**References**
MCS/AAO	0.73	C_H/C_L=50	3
PPSU-Py	0.77	C_H/C_L=50	4
MXene/PS-b-P_2VP	0.78	C_H/C_L=50	5
SNF/AAO	0.79	C_H/C_L=50	6
Mxene/BN	0.82	C_H/C_L=50	7
ZGDHM	0.85	C_H/C_L=50	8
MoS_2	0.87	C_H/C_L=50	9
MC/AAO/MS	0.91	C_H/C_L=50	10
MXene/ZIF-8	0.91	C_H/C_L=50	11
BHMXM	0.94	C_H/C_L=50	12
MXene/AAO/Nafion	0.95	C_H/C_L=50	This work

Table S5. Comparison of the various nanofluidic devices performance for the salinity gradient energy conversion.

Membrane	Power density (W/m^2)	Test Condition	References
SNF/AAO	2.67	C_H/C_L=500	6
UiO-66-NH_2@ANM	7.12	C_H/C_L=500	13
BDA/TAM	7.33	C_H/C_L=500	14
MXene/PS-b-P_2VP	12.4	C_H/C_L=500	5
KANF	15	C_H/C_L=500	15
MoS_2	15.6	C_H/C_L=500	9
BHMXM	17.8	C_H/C_L=500	12
GOM	18.8	C_H/C_L=500	16
CS/SA	19.41	C_H/C_L=500	17
SPEEK	20.2	C_H/C_L=500	18
EGO	20.3	C_H/C_L=500	19
BCP-SA	22.4	C_H/C_L=500	20
ICM	23.57	C_H/C_L=500	21
Cu-TCPP	25.54	C_H/C_L=500	22
COF@ANM	27.8	C_H/C_L=500	23
SPPO/PANI	28.2	C_H/C_L=500	24
p-BCPs	30.8	C_H/C_L=500	25
PAMPS@ANM	48.2	C_H/C_L=500	26
MXCT	49.0	C_H/C_L=500	27
MXene/AAO/Nafion (without light irradiation)	47.9	C_H/C_L=500	This work
MXene/AAO/Nafion (with light irradiation)	65.6	C_H/C_L=500	This work

Table S6. Comparison of the voltage of 10-units with previously reported devices at a salinity gradient of 50-fold NaCl.

Membrane	Voltage	References
SPPO/PANI	0.8	24
R-RC/P-CNTS	1.03	28
PNIPAM-g-sCC	1	29
Layered Membrane	1.1	30
GO/ANF	1.14	31
V-NbP	1.15	32
KANF	1.2	15
Cu-TCPP	1.25	22
NMIM	1.26	33
ABN	1.32	34
2D-HM	1.36	35
Mxene/AAO/Nafion	1.47	This work

References

1 D. K. Kim, C. H. Duan, Y. F. Chen and A. Majumdar, Power generation from concentration gradient by reverse electrodialysis in ion-selective nanochannels, *Microfluid. Nanofluid.*, 2010, **9**, 1215-1224.

2 Z. Q. Li, G. L. Zhu, R. J. Mo, M. Y. Wu, X. L. Ding, L. Q. Huang, Z. Q. Wu and X. H. Xia, Light-Enhanced Osmotic Energy Harvester Using Photoactive Porphyrin Metal-Organic Framework Membranes, *Angew. Chem. Int. Ed.*, 2022, **61**, e202202698

3 S. Zhou, L. Xie, X. F. Li, Y. N. Huang, L. P. Zhang, Q. R. Liang, M. Yan, J. Zeng, B. L. Qiu, T. Y. Liu, J. Y. Tang, L. P. Wen, L. Jiang and B. Kong, Interfacial Super-Assembly of Ordered Mesoporous Carbon-Silica/AAO Hybrid Membrane with Enhanced Permselectivity for Temperature-and pH-Sensitive Smart Ion Transport, *Angew. Chem. Int. Ed.*, 2021, **60**, 26167-26176.

4 X. B. Zhu, J. D. Zhong, J. R. Hao, Y. Z. Wang, J. J. Zhou, J. W. Liao, Y. J. Dong, J. H. Pang, H. B. Zhang, Z. Z. Wang, W. Zhang, W. T. Zheng, Z. H. Jiang, Y. H. Zhou and L. Jiang, Polymeric Nano-Blue-Energy Generator Based on Anion-Selective Ionomers with 3D Pores and pH-Driving Gating, *Adv. Energy Mater.*, 2020, **10**, 2001552.

5 X. B. Lin, P. Liu, W. W. Xin, Y. F. Teng, J. J. Chen, Y. D. Wu, Y. F. Zhao, X. Y. Kong, L. Jiang and L. P. Wen, Heterogeneous MXene/PS-b-P2VP Nanofluidic Membranes with Controllable Ion Transport for Osmotic Energy Conversion, *Adv. Funct. Mater.*, 2021, **31**, 2105013.

6 W. W. Xin, Z. Zhang, X. D. Huang, Y. H. Hu, T. Zhou, C. C. Zhu, X. Y. Kong, L. Jiang and L. P. Wen, High-performance silk-based hybrid membranes employed for osmotic energy conversion, *Nat. Commun.*, 2019, **10**, 3876

7 G. L. Yang, D. Liu, C. Chen, Y. J. Qian, Y. Y. Su, S. Qin, L. Z. Zhang, X. G. Wang, L. Sun and W. W. Lei, Stable $Ti_3C_2T_X$ MXene-Boron Nitride Membranes with Low Internal Resistance for Enhanced Salinity Gradient Energy Harvesting, *ACS Nano*, 2021, **15**, 6594-6603.

8 K. T. Huang, W. H. Hung, Y. C. Su, F. C. Tang, L. D. Linh, C. J. Huang and L. H. Yeh, Zwitterionic Gradient Double-Network Hydrogel Membranes with Superior Biofouling Resistance for Sustainable Osmotic Energy Harvesting, *Adv. Funct. Mater.*, 2023, **33**, 2211316.

9 C. C. Zhu, P. Liu, B. Niu, Y. N. Liu, W. W. Xin, W. P. Chen, X. Y. Kong, Z. Zhang, L. Jiang and L. P. Wen, Metallic Two-Dimensional MoS_2 Composites as High-Performance Osmotic Energy Conversion Membranes, *J. Am. Chem. Soc.*, 2021, **143**, 1932-1940.

10 S. Zhou, L. Xie, X. Zhang, M. Yan, H. Zeng, K. Liang, L. Jiang and B. Kong, Super-Assembled Multi-Level Asymmetric Mesochannels for Coupled Accelerated Dual-Ion Selective Transport, *Adv. Mater.*, 2022, **35**, 2208903.

11 J. L. Zhou, J. R. Hao, R. Wu, L. Y. Su, J. Wang, M. Qiu, B. Bao, C. Y. Ning, C. Teng, Y. H. Zhou and L. Jiang, Maximizing Ion Permselectivity in MXene/MOF Nanofluidic Membranes for High-Efficient Blue Energy Generation, *Adv. Funct. Mater.*, 2022, **32**, 2209767.

12 L. Ding, M. T. Zheng, D. Xiao, Z. H. Zhao, J. Xue, S. Q. Zhang, J. Caro and H. H. Wang, Bioinspired $Ti_3C_2T_x$MXene-Based Ionic Diode Membrane for High-Efficient Osmotic Energy Conversion, *Angew. Chem. Int. Ed.*, 2022, **61**, e202206152.

13 Y. C. Liu, L. H. Yeh, M. J. Zheng and K. C. W. Wu, Highly selective and high-performance osmotic power generators in subnanochannel membranes enabled by metal-organic frameworks, *Sci. Adv.*, 2021, **7**, eabe9924.

14 C. Wang, J. D. Tang, L. Y. Li, J. H. Wan, Y. C. Ma, Y. H. Jin, J. B. Liu, H. Wang and Q. Q. Zhang, Ultrathin Self-Standing Covalent Organic Frameworks toward Highly-Efficient Nanofluidic Osmotic Energy Generator, *Adv. Funct. Mater.*, 2022, **32**, 2204068.

15 L. Ding, D. Xiao, Z. H. Zhao, Y. Y. Wei, J. Xue and H. H. Wang, Ultrathin and Ultrastrong Kevlar Aramid Nanofiber Membranes for Highly Stable Osmotic Energy Conversion, *Adv. Sci.*, 2022, **9**, 2202869.
16 Y. J. Qian, D. Liu, G. L. Yang, L. F. Wang, Y. C. Liu, C. Chen, X. G. Wang and W. W. Lei, Boosting Osmotic Energy Conversion of Graphene Oxide Membranes via Self-Exfoliation Behavior in Nano-Confinement Spaces, *J. Am. Chem. Soc.*, 2022, **144**, 13764-13772.
17 G. S. Bian, N. Pan, Z. H. Luan, X. Sui, W. X. Fan, Y. Z. Xia, K. Y. Sui and L. Jiang, Anti-Swelling Gradient Polyelectrolyte Hydrogel Membranes as High-Performance Osmotic Energy Generators, *Angew. Chem. Int. Ed.*, 2021, **60**, 20294-20300.
18 Y. Y. Zhao, J. Wang, X. Y. Kong, W. W. Xin, T. Zhou, Y. C. Qian, L. S. Yang, J. H. Pang, L. Jiang and L. P. Wen, Robust sulfonated poly (ether ether ketone) nanochannels for high-performance osmotic energy conversion, *Natl. Sci. Rev.*, 2020, **7**, 1349-1359.
19 K. R. Bang, C. Kwon, H. Lee, S. Kim and E. S. Cho, Horizontally Asymmetric Nanochannels of Graphene Oxide Membranes for Efficient Osmotic Energy Harvesting, *ACS Nano*, 2023, **17**, 10000-10009.
20 C. Li, L. P. Wen, X. Sui, Y. R. Cheng, L. C. Gao and L. Jiang, Large-scale, robust mushroom-shaped nanochannel array membrane for ultrahigh osmotic energy conversion, *Sci. Adv.*, 2021, **7**, eabg2183.
21 W. P. Chen, T. D. Dong, Y. Xiang, Y. C. Qian, X. L. Zhao, W. W. Xin, X. Y. Kong, L. Jiang and L. P. Wen, Ionic Crosslinking-Induced Nanochannels: Nanophase Separation for Ion Transport Promotion, *Adv. Mater.*, 2021, **34**, 2108410.
22 J. Wang, Z. Y. Song, M. L. He, Y. C. Qian, D. Wang, Z. Cui, Y. Feng, S. Z. Li, B. Huang, X. Y. Kong, J. M. Han and L. Wang, Light-responsive and ultrapermeable two-dimensional metal-organic framework membrane for efficient ionic energy harvesting, *Nat. Commun.*, 2024, **15**, 2125.
23 M. Y. Gao, M.-J. Zheng, A. F. M. El-Mahdy, C.-W. Chang, Y.-C. Su, W.-H. Hung, S.-W. Kuo and L.-H. Yeh, A bioinspired ionic diode membrane based on sub-2 nm covalent organic framework channels for ultrahigh osmotic energy generation, *Nano Energy*, 2023, **105**, 108007.
24 X. Y. Zhang, B. H. Wu, H. Q. Wu and P. Y. Wu, Engineering Multiscale Heterostructure as Ionic Diode and Light-Driven Ion Pump for Osmotic-Solar Energy Harvesting, *CCS Chem.*, 2025, **7**, 1383-1395.
25 C. Li, H. M. Jiang, P. X. Liu, Y. Zhai, X. Q. Yang, L. C. Gao and L. Jiang, One Porphyrin Per Chain Self-Assembled Helical Ion-Exchange Channels for Ultrahigh Osmotic Energy Conversion, *J. Am. Chem. Soc.*, 2022, **144**, 9472-9478.
26 Y.-C. Lin, H.-H. Chen, C.-W. Chu and L.-H. Yeh, Massively Enhanced Charge Selectivity, Ion Transport, and Osmotic Energy Conversion by Antiswelling Nanoconfined Hydrogels, *Nano Letters*, 2024, **24**, 11756-11762.
27 W.-H. Lin, T.-Y. Huang, C.-H. Bai, C.-H. Hung, C.-A. Lung, W.-H. Hung, K. Gopinadhan and L.-H. Yeh, Novel ultrastable 2D MOF/MXene nanofluidic membrane with ultralow resistance for highly efficient osmotic power harvesting, *Nano Energy*, 2024, **128**, 109924.
28 B. L. Zhou, Z. W. Lin, Z. J. Xie, X. T. Fu, Z. H. Yuan, C. L. Jiao, X. Z. Qin and D. D. Ye, Scalable fabrication of regenerated cellulose nanohybrid membranes integrating opposite charges and aligned nanochannels for continuous osmotic energy harvesting, *Nano Energy*, 2023, **115**, 108693.
29 X. J. Lin, Y. J. Dong, S. M. Tao, X. Feng, X. J. Wang, T. Song, J. Liu, Z. H. Zhong, Y. C. Wang and H. S. Qi, Temperature-gated nanocellulose membrane for enhanced and controllable osmotic energy harvesting, *Nano Energy*, 2023, **107**, 108156.
30 Z. J. Xie, Z. R. Xiang, X. T. Fu, Z. W. Lin, C. L. Jiao, K. Zheng, M. Yang, X. Z. Qin and

D. D. Ye, Decoupled Ionic and Electronic Pathways for Enhanced Osmotic Energy Harvesting, *ACS Energy Lett.*, 2024, **9**, 2092-2100.
31 J. Chen, W. Xin, W. Chen, X. Zhao, Y. Qian, X. Y. Kong, L. Jiang and L. Wen, Biomimetic Nanocomposite Membranes with Ultrahigh Ion Selectivity for Osmotic Power Conversion, *ACS Cent. Sci.*, 2021, **7**, 1486-1492.
32 J. Safaei, Y. F. Gao, M. Hosseinpour, X. Y. Zhang, Y. Sun, X. Tang, Z. J. Zhang, S. J. Wang, X. Guo, Y. Wang, Z. Chen, D. Zhou, F. Y. Kang, L. Jiang and G. X. Wang, Vacancy Engineering for High-Efficiency Nanofluidic Osmotic Energy Generation, *J. Am. Chem. Soc.*, 2023, **145**, 2669-2678.
33 F. Zhang, J. Y. Yu, Y. Si and B. Ding, Meta-Aerogel Ion Motor for Nanofluid Osmotic Energy Harvesting, *Adv. Mater.*, 2023, **35**, e2302511.
34 C. Chen, D. Liu, L. He, S. Qin, J. M. Wang, J. M. Razal, N. A. Kotov and W. W. Lei, Bio-inspired Nanocomposite Membranes for Osmotic Energy Harvesting, *Joule*, 2020, **4**, 247-261.
35 Z. G. Xiang, Y. Chen, Z. J. Xie, K. Y. Yuan, Y. Shu, P. Chen, H. Q. Wang and D. D. Ye, Sustainable Chitin-Derived 2D Nanosheets with Hierarchical Ion Transport for Osmotic Energy Harvesting, *Adv. Energy Mater.*, 2024, **14**, 2402304.